

Latest Edition

Welcome to the April 2013 edition of TCAD News. In this edition we present the new features and enhancements in the H-2013.03 release of TCAD Sentaurus, which includes a number of important new and updated features addressing the modeling challenges of 10nm FinFET, 3D memory and Si and wide bandgap power devices. For example, new models for melt laser annealing, dislocation engineering and diffusion in III-V semiconductors have been implemented in Sentaurus Process, along with significant robustness and speed improvements in 3D oxidation. A detailed article on Sentaurus Topography highlights important features to support the development of new types of memory cells. In device simulation, updates to band structure and mobility modeling of Ge and SiGe attest to the importance of these materials in future process nodes. The capabilities for simulating GaN and SiC power devices have also been improved. In interconnect reliability modeling, we continue to broaden the applications of Sentaurus Interconnect with the release of new models for creep and swelling, improved accuracy with second order finite elements and updates to fracture mechanics. Over the last two quarters Sentaurus Visual has become the visualization tool of choice for many customers, and in this release we add to its capabilities and flexibility.

I trust that you will find these new enhancements in the H-2013.03 release of TCAD Sentaurus useful for your simulation tasks of exploring, developing, and optimizing a variety of processes and devices. As always, I welcome your feedback and suggestions.

With warm regards,

Terry Ma
Vice President of Engineering, TCAD

Contact TCAD

For further information and inquiries:
tcad_team@synopsys.com

TCAD news

Sentaurus Process

Ion Implantation Enhancements

Automatic Implant Moment Extraction

Sentaurus Process includes several tables of implant moments which cover many species and materials over a wide range of implant conditions in silicon. However, users may occasionally want to use implant parameters outside of the supplied implant tables. In such cases, users can seek access to experimental implant profiles or run Monte Carlo implant simulations. Automatic implant moment extraction then converts these raw profiles into the moments which can be used in analytic implant.

The critical part of automatic extraction of implant moments is the optimization (or least square fit) algorithm, which can be stated as: given a profile or a set of m pairs of data points (x_i, y_i) , optimize the parameter set β of the model function $f(x, \beta)$, so that the sum of the squares of the errors at each point becomes minimal:

$$S(\beta) = \sum_{i=1}^m [y_i - f(x_i, \beta)]^2 \quad (1)$$

Sentaurus Process uses the same optimizer as TSUPREM-4, which implements the popular Levenberg–Marquardt algorithm.

In order to do the moment extraction, the parameters `extract.moments` and `data.` file need to be specified in the `implant` statement. The implant profiles can be fitted to `gaussian`, `pearson`, or `dualpearson` distributions. The default is `dualpearson`. Figure 1 shows an example of an extracted profile compared with the raw data.

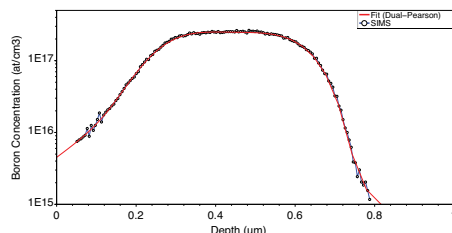


Figure 1: Comparison of the extracted profile (dual-Pearson) with the original raw data.

In This Edition

Sentaurus Process.....	1
Sentaurus Topography.....	7
Sentaurus Device.....	10
Sentaurus Interconnect.....	15
Sentaurus Mesh.....	18
Sentaurus Visual	19
Sentaurus Workbench	20



In order to facilitate the creation of implant tables from Monte Carlo implant data, we have developed a Tcl script **ImplantTableMaker**. This script must be run in interactive mode and requires the input of various implant parameters that are necessary to create a Taurus format implant table. The resulting table is named `<species>_in_<material>_mystandard`.

However, creating a high quality implant table is a difficult task. Since each implant profile is extracted independently, and the Levenberg–Marquardt optimization algorithm can only find the local minima, slightly different profiles may result in totally different implant moments. Interpolation between these moments may not give optimal results. Therefore, while **ImplantTableMaker** may be suitable for creating small tables, the quality of implant tables (especially large tables) cannot be guaranteed.

Implantation with Energy Contamination

Deceleration of the ion beam is often used to obtain the ultra-low energies needed to form ultra-shallow junctions. However, this method leads to the production of neutrals when the ions interact with residual gas molecules in the beam line before the deceleration electrodes. These neutrals will not be affected by the deceleration electric fields and therefore reach the target wafer at higher than desired energies. This effect is known as energy contamination and leads to a deeper than desired dopant depth profile.

This energy contamination implantation is now supported in Sentaurus Process with the parameter `contamination={energy=<n> dose.fraction=<n>}` in the `implant` command, in which a fraction of the nominal dose has a different energy than the specified energy. Sentaurus Process then treats this implantation as two separate implantations. This feature is supported in both analytic and Monte Carlo implant.

New Energy Distribution Model in Plasma Implant

The energetic distribution of different molecular and atomic ions, after extraction from the plasma, can be very complicated. The default model in Sentaurus Process assumes a Gaussian distribution for the the energy of the plasma species. Alternatively, it can be assumed that the energy covers the range from zero to the maximum energy, which is equal to the product of the ion charge multiplied by the extraction voltage. Sentaurus Process allows easy selection and addition of various energy distribution models. In addition to the default Gaussian distribution, Sentaurus Process now implements an alternative model [1]. In this model, the energy distribution, the number of particles having their energy in a given interval, can be written as

$$f(E) = \frac{5}{6E_{max}} \left(\frac{E}{E_{max}} \right)^{-1/6} \quad (2)$$

The energy distribution is normalized and it shows excellent agreement between simulations and experiments for BF₃ plasma implantation [1].

Monte Carlo Implant in Ge and High Mole Fraction Si_{1-x}Ge_x

Sentaurus MC implantation in crystalline germanium has been calibrated based on available experimental data [2,3,4]. The calibration is based mainly on [2] and [3], with reference [4] used just to check the profiles at higher energy. The calibration covers the following energy range:

Boron: 5-140 keV

Arsenic: 20-80 keV

Phosphorus: 20-320 keV

It is noteworthy that due to the heavy mass of germanium, backscattering is much more significant in germanium than in silicon. According to our simulations, there is approximately 15%, 10%, and 5% backscattering at 20, 40, and 80 keV for

boron implant in germanium. However, the data reference [2] do not account for this effect since the SIMS data were normalized to the nominal doses. In order to account for this backscattering effect, we adjusted the doses in simulation to match the actual doses in experiments.

There is good agreement between SIMS and simulations, as shown in Figures 2 and 3. Further improvement is possible if new and more reliable data in expanded parameter space becomes available.

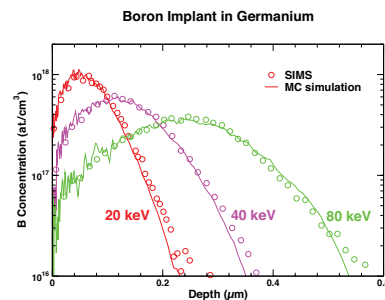


Figure 2: Comparison of MC simulation and SIMS profile for boron implant in germanium.

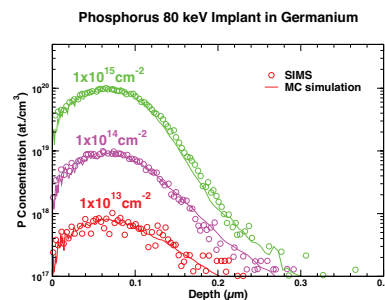


Figure 3: Comparison of MC simulations and SIMS profiles for phosphorus implant in germanium.

Since our MC implantation model for Si_{1-x}Ge_x is based on the interpolation of physical quantities between silicon and germanium (lattice constant, electronic stopping power, etc), more accurate MC implantation results are expected for large mole fraction Si_{1-x}Ge_x.



Diffusion and Oxidation Enhancements

Melt Laser Anneal Model

Melt laser anneal (MLA) is performed with high intensity light for a few hundreds of nanoseconds, which lends this technique the advantages of localized heat diffusion and high dopant activation following resolidification. Insulated gate bipolar transistors (IGBT) are a good example of a device technology whose performance can be improved with MLA. In IGBT processing, after the front side of the device is completed, the collector is formed on the backside of the wafer. With traditional annealing processes the backside processing on wafers of thickness 100 μm or less is limited to low thermal budgets since a few tens of microseconds are sufficient for the heat to reach the front of the wafer. This lowers dopant activation and increases the collector resistance, with attendant detrimental impacts to the switching speed of the device. Melt laser annealing solves this problem [5]. The thermal diffusion and phase change for the melt laser anneal are simulated by solving the temperature and phase equations which are derived by the phase field method [6][7],

$$\rho c_p \frac{\partial T}{\partial t} = \nabla \cdot (\kappa \nabla T) + I \alpha e^{-\int \alpha dx} + \rho L \cdot 30\varphi^2(1-\varphi)^2 \frac{\partial \varphi}{\partial t} \quad (3)$$

$$\frac{\partial \varphi}{\partial t} = \mu \gamma \nabla^2 \varphi - \frac{\mu \gamma}{\delta^2} \varphi(1-\varphi)(1-2\varphi) + \frac{v_{int}(T)}{6\delta} \cdot 30\varphi^2(1-\varphi)^2 + S(T, \varphi) \quad (4)$$

where ρ , c_p , κ and α are the mass density, the specific heat capacity, the thermal conductivity and the absorption coefficient respectively. The specific heat capacity and thermal conductivity are functions of the temperature and phase, as shown in figure 4. L , μ , γ and δ are the latent heat, the melting interface mobility, the surface tension, and the interface thickness, respectively.

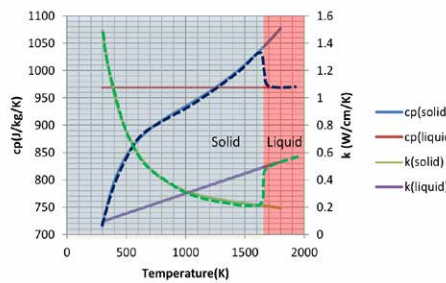


Figure 4: Specific heat capacity and thermal conductivity of silicon depending on temperature and phase

The seed term S induces the initial solid-to-liquid phase change. The interface response function v_{int} is modeled by the Frenkel-Wilson law [8] and the Fulcher-Vogel expression [9] by assuming the atomic transport due to random fluctuation in the local free volume follows,

$$v_{int}(T) = v_0 e^{-\frac{B}{k(T-T_g)}} \left(1 - e^{-\frac{\rho L / C_{max}}{k T T_M} (T - T_M)} \right) \quad (5)$$

where C_{max} and T_M are the lattice density and the melting point respectively. The spatial variation of temperature is not negligible within the diffusion length because the dopant diffusion in liquid is very fast (~7 to ~8 orders faster than in the solid). The chemical potential depends on the phase which results in the dopant segregation at solid/liquid interface. Thus, the dopant diffusion equations must be fully coupled with the temperature and phase equations.

$$\frac{\partial C}{\partial t} = \nabla \cdot \left(\left(D(T, \varphi) e^{-\frac{\varphi E_s + 16\varphi^2(1-\varphi)^2 E_i}{kT}} \right) \nabla \left(C e^{\frac{\varphi E_s + 16\varphi^2(1-\varphi)^2 E_i}{kT}} \right) \right) \quad (6)$$

where $D(T, \varphi)$ is the diffusivity varying on the local temperature and phase; E_s and E_i are the chemical potential difference at a solid and interface regions to a liquid region, respectively.

Figure 5 shows the comparison of the simulation results and SIMS data for phosphorus diffusion with several different fluence conditions.

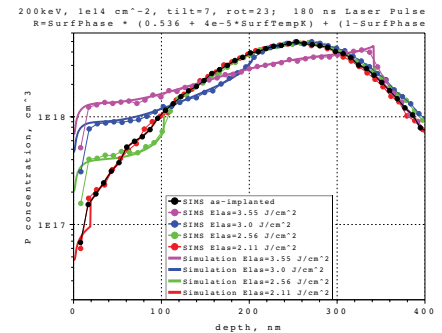


Figure 5: Simulated and SIMS phosphorus profiles for four MLA fluence conditions.

Figure 6 shows the Net active profiles of 600V IGBT with backside field-stop and p+layer activation for conventional anneal at 500C for 1hr using melt laser anneal.

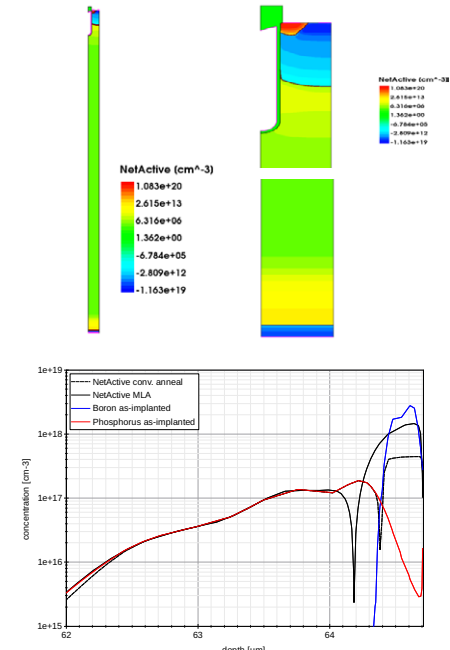


Figure 6: Net active doping profiles in IGBT.

The higher boron activation in the melt laser anneal reduces the resistance in the device significantly, thereby improving the maximum allowable peak current in the device as seen in figure 7.

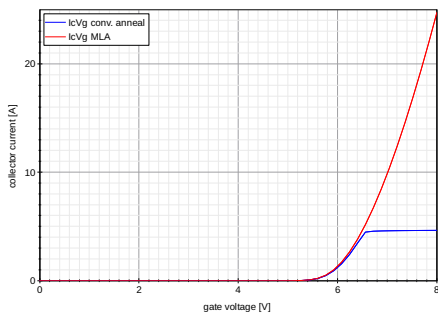


Figure 7: IGBT collector current for conventional anneal (blue) and MLA (red). The higher activation in the MLA process leads to higher current.

Diffusion in III-V Semiconductors

Stress engineering has been applied successfully to enhance the carrier mobility in CMOS. However, further enhancing carrier mobility becomes challenging for technologies beyond the 10nm node. Using materials other than silicon in the channel region is one option being investigated. The electron mobility in InGaAs is larger than $10\text{K cm}^2\text{V}^{-1}\text{s}^{-1}$ and that the hole mobility in germanium is $1900\text{ cm}^2\text{V}^{-1}\text{s}^{-1}$. These mobility values are about 10 times larger than in silicon. However modeling dopant diffusion in III-V semiconductors such as InGaAs is very challenging due to the complexity of reactions. From the point of view of process simulation and the calibration of its model parameters, it is not practical to implement all possible reactions into the equation system. Thus, reasonable assumptions must be made to reduce the number of equations to be solved. Four energetically favorable assumptions are made as follows:

1. point-defects diffuse by the 2nd nearest neighbor hopping [1];
2. group-II dopants react only with group-III point-defects;
3. group-VI dopants react only with group-V point-defects;
4. no antisite defects, that is, no group-III atom occupies a group-V site, and vice versa.

In addition, three other assumptions are applied:

1. vacancies are not differentiated by III and V vacancies, which means that, for example, vacancies generated by kicking out indium or gallium substitutional atoms in InGaAs are identical;
2. point-defects pairing with dopants are not differentiated by III and V point-defects, implying that, for example, Be-I_{Ga} pair is assumed to be identical to Be-I_{In} pair in InGaAs;
3. for a group-IV dopant A and a point-defect X, the reaction between the dopant-defect pairs, AX_{III} and AX_V, is in local equilibrium so that the ratio of equilibrium substitutional concentration at group III to group V is given by a physical parameter.

With these seven assumptions, the continuum diffusion model in III-V compound materials can be reduced to a 8-stream model for a binary compound material, a 11-stream model for a ternary compound material, and a 13-stream model for a quaternary compound material. The auto compensation due to the amphoteric behavior of group-IV dopants is implicitly taken into account by solving the equations for substitutional concentration solutions at group-III and group-V sites as shown in figure 8.

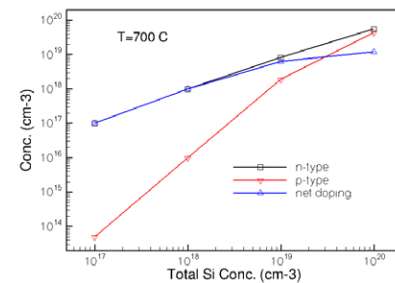


Figure 8: Illustration of the amphoteric behavior of silicon dopants in III-V materials. At high concentrations the occupation of group-III and group-V sites approaches each other, leading to a decrease in the net doping.

The physical parameter values for ternary and quaternary compound materials are automatically calculated by the mole-fraction dependent interpolation from the parameter values of binary compound materials. With the mole-fractions x and y this becomes,

$$P_{III_A(x)III_B(1-x)V_D} = x \cdot P_{III_AV_D} + (1 - x) \cdot P_{III_BV_D}$$

for ternary $A_{(x)}B_{(1-x)}D$

$$P_{III_A(x)III_B(y)III_C(1-x-y)V_D} =$$

$$x \cdot P_{III_AV_D} + y \cdot P_{III_BV_D} + (1 - x - y) \cdot P_{III_CV_D}$$

for quaternary $A_{(x)}B_{(y)}C_{(1-x-y)}D$

$$P_{III_A(x)III_B(1-x)V_C(y)V_D(1-y)} =$$

$$x \cdot P_{III_AV_C} + x(1 - y) \cdot P_{III_AV_D}$$

$$+ (1 - x)y \cdot P_{III_BV_C} + (1 - x)(1 - y) \cdot P_{III_BV_D}$$

for quaternary $A_{(x)}B_{(1-x)}C_{(y)}D_{(1-y)}$

The electrical equation system has been revised so as to correctly take the discontinuous electron affinity and the energy bandgap at hetero-junctions into account (Fig. 9).

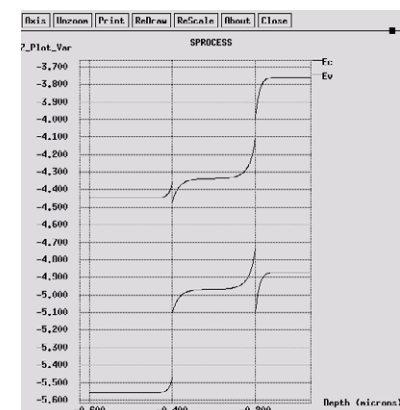


Figure 9: Conduction and valence energy band diagram of N-InP/N-In_{0.53}Ga_{0.47}As/P-InP.



The dopant distribution near a heterojunction is affected by not only the chemical potential difference but also the strong electric field due to misaligned band edges. In H-2013.03, many physical parameters haven't yet been calibrated yet so that the lack of simulation accuracy is expected. This limitation will be addressed in future releases.

Progress in 3-D Oxidation

3D oxidation has been sped up, with most examples showing about a factor of two speed improvement. The speed improvements stem from a better mesh motion algorithm and a more efficient way to call the box method library. A long oxidation step that previously took an entire day to simulate can now finish overnight.

To support 3D oxidation, our MovingMesh algorithm uses body-fitted tetrahedral meshes, and material interfaces are represented explicitly as triangulated surfaces. Each surface mesh conforms to the neighboring bulk meshes. In our approach, the bulk mesh and the material boundaries move together and remain conformal throughout the simulation. Our design was motivated by the need for accurate segregation, accurate dopant profile, and dose conservation.

In the past 3D oxidation encountered difficulties in maintaining the quality of tetrahedrons in the bulk, the quality of triangles in the interfaces, and the quality of the underlying geometry, especially during long oxidation processes. After many years of research, we have developed a set of tools that solve these problems, so that the simulation can maintain reasonable time steps and run to completion with accurate, conservative, and trustworthy results.

To maintain quality of the underlying geometry, we developed a combination of algorithms which produces smooth surfaces when needed. The algorithms are multi-threaded and have been designed to

efficiently handle the complex shapes that develop during the oxidation process.

In H-2013.03 we improved the surface algorithms to be able to generate more points near high-curvature areas and quickly generate a sparse set of points around flat areas. The speed and stability of these algorithms was also improved in the H-2013.03 release.

We also simplified the input deck in H-2013.03 by letting the 2D (TS4Mesh) and the 3D (MovingMesh) algorithms share the same set of parameters for mesh refinement and coarsening. Users can easily switch from 2D to 3D.

Figure 10 shows an example of the LOCOS oxidation with 120nm nitride mask corner at 950C under 6.5l/min O₂ and 6l/min H₂ flow for 4.5 hours. The grown oxide thickness is 590nm with the expected bird's beak effect. The CPU time is 7 hours on an Intel Xeon 3 GHz computer with 16 GB of RAM.

Figure 11 shows an example of the snowplow effect. Phosphorus preferably segregates into the silicon side at the silicon/oxide interface with the pile-up expected to be strongest at the 3D convex corner. This example shows a wet oxidation at 1150C for 50 minutes. The initial wafer is uniformly phosphorus doped at $5 \times 10^{16} \text{ cm}^{-3}$. For clarity, the grown 720nm oxide is shown as outline.

Figure 12 shows an example of a transistor process flow. The pictures show trench oxidation, gate oxidation followed by poly re-oxidation, and implantation. The first two pictures plot the oxidant concentration. The last picture plots the dopant profile. The running time for each oxidation step took about four hours (trench oxidation), one hour (gate oxidation), and one hour (poly re-oxidation). The running time for the entire flow is about 12 hours on a Intel Xeon 2.6GHz computer with 72 GB of RAM compared to more than 28 hours in the previous release.

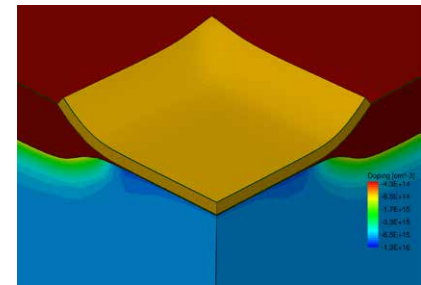


Figure 10: LOCOS oxidation of a mask corner.

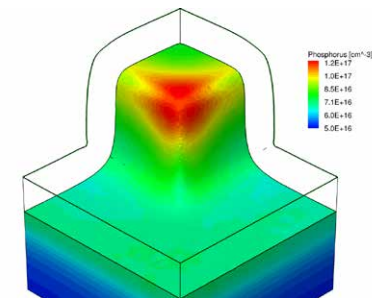


Figure 11: Phosphorus pile-up on the silicon side of the silicon/oxide interface.

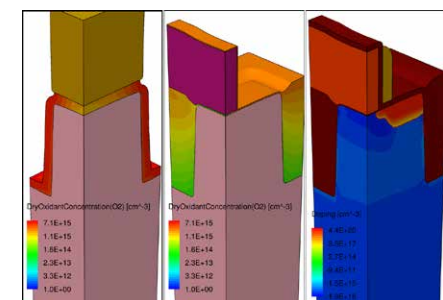


Figure 12: Process flow with trench oxidation (left), gate oxidation followed by poly re-oxidation (center) and implantation (right).



Dislocation Positioning Through Energy Minimization

Dislocation engineering allows dislocations of interest to be introduced at selected positions in the crystalline material and arranged in specified groups. Stress analysis with the finite element method has been used to study the effect and the distribution of the edge dislocations.

Sentaurus Process includes now a prototyping model to determine the locations of edge dislocations by minimizing the elastic strain energy. The total elastic strain energy is calculated from the edge dislocation-induced stress and depends on the location of each edge dislocation. The magnitude and orientation of the edge dislocations stay the same during the minimization. The core coordinates used to define the edge dislocation serve as the initial guess. To determine the movement of the edge dislocations, the gradient of the total elastic strain energy from the discrete integral over all elements is used. The minimization yields the final coordinates of the edge dislocations and the corresponding total elastic strain energy.

Our model is a continuum model that requires fine mesh for accurate dislocation induced stress field and smooth elastic strain energy function.

Power Device Mode

Process simulation flows for power device technologies usually require long annealing times with thick oxide growth compared to CMOS process flows. Therefore simpler diffusion models without clustering are used to simulate power device process flows. Sentaurus Process H-2013.03 employs a new command called “PowerDeviceMode” for defining simulation flows applicable to power devices, where diffusion models are automatically set to Fermi models with simple activation models for boron, phosphorus, arsenic, antimony, and indium in silicon. The command also turns off the point defect equations, dopant, and defect clusters and relaxes time step control to

allow bigger diffusion steps. It reduces the mesh refinement around the interface as well. The command provides up to 50% performance improvement for certain applications, without compromising the accuracy of solutions.

Lattice Kinetic Monte Carlo and Kinetic Monte Carlo Updates

Generic Materials for Kinetic Monte Carlo

As for the continuum mode in release G-2012.06, the kinetic Monte Carlo (KMC) and lattice kinetic Monte Carlo (LKMC) mode in H-2013.03 has been generalized to support crystalline materials other than silicon. Several models have been improved to allow users to implement their own defined materials in KMC. All the physical mechanisms available for silicon and SiO_2 are available for user-defined materials. Moreover, the substrate material germanium and its native oxide GeO_2 have been added as predefined materials. All the models available for silicon are also available for germanium, but with a set of parameters for germanium. This allows the simulation of both pure germanium material and germanium alloys with a GeO_2 interface. A basic calibration has been performed, and default parameters for material properties, implant damage accumulation, solid phase epitaxial regrowth, point defect evolution, and dopant (arsenic, boron, and phosphorus) diffusion, activation and segregation at the GeO_2 interface have been introduced to the Sentaurus Process parameter database. The calibration follows mainly the one for continuum process simulation, being based on the same literature. Boron, for instance, diffuses very little and has a low solubility in germanium, but good activation can be achieved by pre-amorphization and recrystallization of boron implanted profiles as seen in figure 13. In contrast, phosphorus has a higher solubility but diffuses very strongly via charged vacancies in germanium, see figure 14.

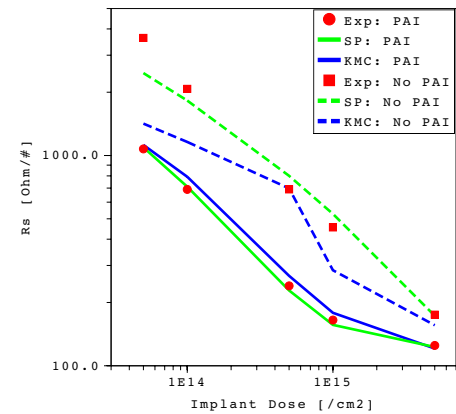


Figure 13: Measured sheet resistance [11] and corresponding simulation results of Sentaurus Process continuum and KMC for B (2keV) implantation into Ge followed by annealing at 400C for 1h, with and without Ge pre-amorphization implant (PAI). B activation is significantly enhanced in case of PAI.

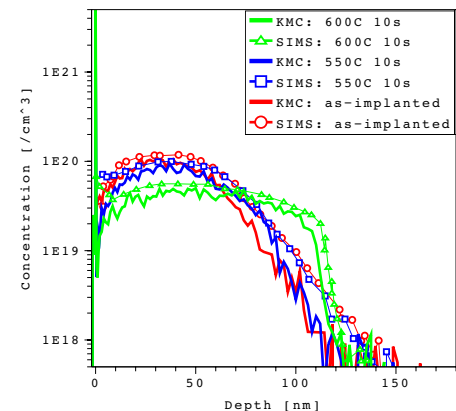


Figure 14: SIMS [12] and KMC simulation results for P (40keV $6\text{e}14 \text{ cm}^{-2}$) implantation into Ge followed by rapid thermal annealing. P shows strong diffusion at temperatures above 550C.

Material Alloying

In addition, Sentaurus Process KMC has been enhanced to allow materials containing an alloy element to be treated in a quasi-atomistic framework. So far, only germanium was allowed as alloy, in the case of SiGe. With release H-2013.03, any element can be selected as alloy. Such an alloy element is specified using the Alloy parameter of the material specification. The alloy is used to correct all activation energies for diffusion, emission, and activation-related processes as a term linear on the alloy concentration.



Percolation Models

A new percolation model has been added to the KMC model library. In a percolation event, an impurity can react with any other defect in its neighborhood without the need for diffusion. In this aspect, it can simulate the reactions that occur through distortions in the lattice but without the need for migration of particles. The percolation rate, that is, the frequency at which the particle attempts to interact with any valid defect in its neighborhood, is defined as $V_{per} = P_{per} \exp(-E_{per}/k_B T)$, where P_{per} and E_{per} are the prefactors and activation energy for percolation, specified as input parameters. Percolation only applies to substitutional dopants or impurities. It can provide an extra mechanism for dopant deactivation at very high concentrations.

References

- [1] A. Burenkov, et al., "Simulation of BF₃ Plasma Immersion Ion Implantation into Silicon," in 19th International Conference on Ion Implantation Technology (IIT), Valladolid, Spain, pp. 233–236, June 2012.
- [2] Suzuki, et al., "Ion-Implanted Impurity Profiles in Ge Substrates and Amorphous Layer Thickness Formed by Ion Implantation", IEEE Trans. Electron Device, VOL. 56, NO. 4, pp. 627-633, APRIL 2009.
- [3] Wittmann, et al., "A study of ion implantation into crystalline germanium", Solid-State Electronics, vol. 51, pp. 982–988, 2007.
- [4] Suh, et al., "Modeling of Boron and Phosphorus Implantation Into (100) Germanium", IEEE Trans. Electron Device, VOL. 52, NO. 1, pp. 91-98, January 2005.
- [5] T. Gutt and H. Schulze, "Deep melt activation using laser thermal annealing for IGBT thin wafer technology", ISPSD, pp.29-32 (2010).
- [6] C. Beckermann, H.J. Diepers, I. Steinbach, A. Karma and X. Tong, "Modeling Melt Convection in Phase-Field Simulations of Solidification," J. Comp. Phys., 154, pp.468-496 (1999).
- [7] A. Karma and W. Rappel, "Quantitative phase-field modeling of dendritic growth in two and three dimensions", Phys. Rev. E, 57, pp.4323-4349 (1998)
- [8] R. F. Wood, G. A. Geist, "Modeling of Nonequilibrium Melting and Solidification in Laser-Irradiated Materials", Phys. Rev. B, 34 (1986)
- [9] S. R. Stiffler, P. V. Evans and A. L. Greer, "Interfacial transport kinetics during the solidification of silicon", Acta Metall. Mater. 40 pp.1617-1622 (1992)
- [10] J. F. Wager, "Energetics of self-diffusion in GaAs", JAP, 69(5) (1991)
- [11] B.R. Yates et al., "Anomalous activation of shallow B+ implants in Ge", Materials Letters 65 (2011) 3540-3543
- [12] V. Mazzocchi et al., "Experimental Investigation of the Impact of Implanted Phosphorus Dose and Anneal on Dopant Diffusion and Activation in Germanium", Mater. Res. Soc. Symp. Proc. Vol. 1070, 1070-E01-08 (2008).

Sentaurus Topography: The Next Step in Feature-Scale Topography Simulation

Sentaurus Topography 3D is a three-dimensional level set-based simulator for evaluating and optimizing critical topography steps such as etching and deposition. Three-dimensional (3D) structures composed of an arbitrary number of materials can be handled, and several physical effects can be modeled for multiple chemical species involved in the process [1].

In addition to being capable of handling arbitrary 3D structures, Sentaurus Topography 3D can also run in two-dimensional (2D) mode to efficiently simulate structures that are invariant along one direction. Since almost all models can be run in both 2D and 3D mode, the 2D mode is also useful for performing fast calibrations.

Physical Modeling Capabilities

Sentaurus Topography 3D makes it possible to use physical models of etching, deposition, and simultaneous etching and deposition processes, since it allows the evolution of the feature under investigation to depend on the interaction of the particles present in the reactor with the exposed surface of the wafer itself. This approach is specific to Sentaurus Topography 3D and allows this tool to capture important effects—for example, aspect ratio-dependent etch rate, loading effects, microtrenching, void formation—which cannot be modeled in Sentaurus Process [1].

Sentaurus Topography 3D can compute not only direct fluxes (that is, fluxes of

particles reaching the surface directly from the source), but also indirect fluxes (that is, fluxes of particles reaching the surface after interacting with it, even multiple times), as shown in Figure 1.

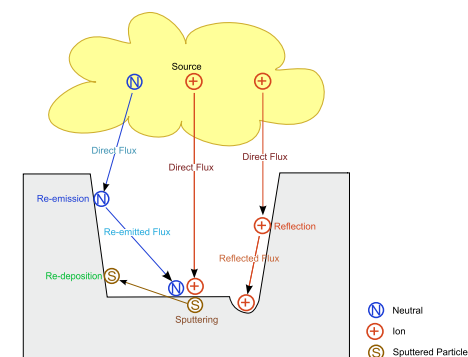


Figure 1: Particle-surface interaction mechanisms supported by Sentaurus Topography 3D.

Each chemical species relevant for the simulated process is modeled as a flux of particles. Two kinds of flux, neutrals and ions, are available, which differ for the surface interaction mechanisms and the angular distributions they support. Neutrals can either stick to the surface when they reach it, or they can be re-emitted according to their sticking coefficient (re-emission). Ions can react on the surface or, depending on their incoming direction, can be reflected (reflection). Moreover, ions can sputter atoms off the surface (sputtering), and sputtered material can be re-deposited (re-deposition).

Neutrals always have isotropic angular distributions in the reactor, whereas ion angular distributions (IADs) are typically narrow because the positively charged ions are accelerated towards the wafer surface. Ion distributions obtained from measurements or plasma simulators can be input to Sentaurus Topography 3D.

Crystal orientation-dependent rates also allow the modeling of anisotropic etching and deposition processes, such as KOH silicon etching.

In addition, Sentaurus Topography 3D provides several commands to conveniently create 2D and 3D structures and to manipulate existing geometries as well as to extract data and measurements from the computed results. As an example, the `extract` command allows users to generate 1D and 2D cuts and to measure critical dimensions of the structure of interest [1].

The Rate Formula Module

Even though Sentaurus Topography 3D provides a set of several built-in models for etching, deposition, and simultaneous etching and deposition processes, users can define their own models using either the physical model interface (PMI) or the rate formula module (RFM). In particular, the RFM represents a very flexible and powerful way to specify user-defined models. It does not require any C++ programming knowledge,

but it is completely based on the Sentaurus Topography 3D command language [1].

Models with arbitrary numbers of neutral and ion fluxes can be created with the RFM, and any supported interaction mechanism between the particles and the surface can be enabled for each flux. In addition, arbitrarily shaped IADs, yield, and reflection functions can be used in RFM models. User-defined parameters and standard mathematical functions are also available for the definition of the rate formula. Therefore, the RFM allows Sentaurus Topography 3D to be used as a flexible platform to develop and run models of topographic processes.

In the following, RFM modeling and simulation of a two-step topographic process are demonstrated. The first step consists of simultaneous etching and deposition to drill a trench, which is then filled with aluminum in the second step.

Simultaneous Etching and Deposition

The model used for this step involves a neutral (N) and an ion (I) flux. Re-emission of neutrals is taken into account as well as ion sputtering and reflection. Yield and reflection functions are specified according to Yamamura's model [2] and Mizuno's model [3], respectively. In addition, the material `Anyinsulator` is deposited during the process to model polymer deposition.

A cut view of the initial structure, made of silicon and nitride layers embedding an aluminum contact and covered by a photoresist mask, is shown in Figure 3(a).

Since Sentaurus Topography 3D allows you to exploit structure symmetries and to reduce the simulation domain, only one-quarter of the structure needs to be included in the simulation. Then, the original structure can be obtained by a mirroring operation with the `extend_structure` command [1].

In the modeled process, the material `Anyinsulator` is deposited on all materials. Etching of nitride and silicon occurs due to an ion-enhanced mechanism. Accordingly, the rate formula for nitride and silicon reads:

$$R_m = -ER_m \frac{\sigma_{N,m} N_0 I_0 \Gamma_{N,tot} \Gamma_{I,tot}}{\sigma_{N,m} N_0 \Gamma_{N,tot} + I_0 \Gamma_{I,tot}} \\ + DR \sigma_{N,m} N_0 \Gamma_{N,tot}$$

where $\Gamma_{N,tot}$ and $\Gamma_{I,tot}$ are the neutral and ion total fluxes, respectively; the subscript m denotes a material-dependent parameter; $\sigma_{N,m}$, ER_m , DR, and R_m are the sticking coefficient, the etching rate, the deposition rate, and the net evolution rate, respectively. N_0 and I_0 are material-independent parameters representing the absolute neutral and ion fluxes, respectively.

Since the other materials of the structure are etched by ion sputtering, their rate formula is the following:

$$R_m = -ER_m I_0 \Gamma_{I,sputtered} + DR \sigma_{N,m} N_0 \Gamma_{N,tot}$$

where $\Gamma_{I,sputtered}$ is the sputtered flux. Figure 2 shows the Sentaurus Topography 3D commands to specify these rate formulas in the RFM model definition.

```
add_formula model=m name=neutrals subexpression="N_0() * total_flux(N) * sticking(N)" 
add_formula model=m name=ions subexpression="I_0() * total_flux(I)" 
add_formula model=m material=Nitride expression="-rate() * (checked_div(neutrals()) * ions(), \
    neutrals() + ions(), 0.) + depo_rate() * neutrals()" 
add_formula model=m material=Silicon expression="-rate() * (checked_div(neutrals()) * ions(), \
    neutrals() + ions(), 0.) + depo_rate() * neutrals()" 
add_formula model=m expression="-rate() * I_0() * sputtered_flux(I) + depo_rate() * neutrals()"
```

Figure 2: RFM syntax to define rate formulas describing the simultaneous etching and deposition step.

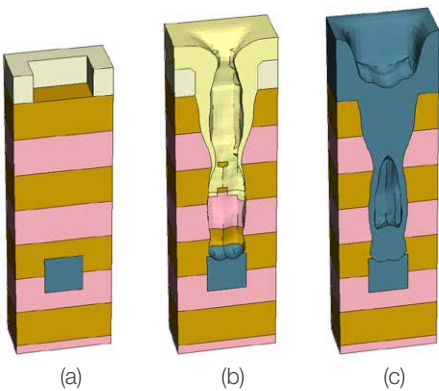


Figure 3: (a) Initial structure, (b) structure obtained after simultaneous etch and deposition, and (c) structure obtained after deposition.

The trench obtained after a 3 minute long process is shown in Figure 3(b). Microtrenching due to ion reflection can be observed at the bottom as well as a complex-shaped trench profile caused by the interactions of ion and neutral particles with the surface, as specified by the defined RFM model.

Deposition of Aluminum

After removing the deposited polymer and the photoresist mask with the `remove_material` command [1], the etched trench is filled with aluminum.

A plasma-enhanced chemical vapor deposition process is modeled with an RFM model involving a neutral and an ion flux. Re-emission is modeled for neutrals; whereas, only reflection is taken into account for ions. Therefore, the deposition rate R is given by the following formula:

$$R = DR \left((1 - A) \sigma_{N,m} N_0 \Gamma_{N,tot} + A I_0 \Gamma_{I,tot} \right)$$

where A is a parameter controlling the weight of the ion flux with respect to the neutral one.

The obtained result is displayed in Figure 3(c) and clearly shows how Sentaurus Topography 3D can be used to capture and investigate void formation.

Integration with other Sentaurus Tools

Functionalities of Sentaurus Topography 3D are accessible from within Sentaurus Process and Sentaurus Interconnect, and Sentaurus Lithography can be run using Sentaurus Topography 3D commands.

In addition, Sentaurus Topography 3D is able to read TDR boundary files produced by other tools as well as its output structures can be loaded by other Sentaurus tools. Therefore, a full manufacturing process involving critical topographic steps can be simulated and optimized using Sentaurus TCAD.

Mechanical Stress Simulation with Sentaurus Interconnect

Figure 4 shows the result of a mechanical stress simulation of vertical silicon fins with unequal oxide deposition on their sidewalls using Sentaurus Topography 3D and Sentaurus Interconnect. Sentaurus Interconnect called Sentaurus Topography 3D to simulate the low pressure chemical vapor deposition (LPCVD) of oxide, and then computed the mechanical stress in the obtained structure.

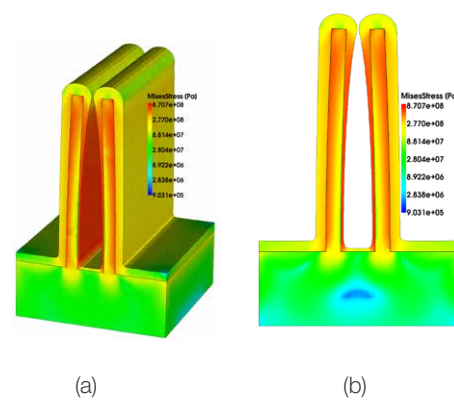


Figure 4: Mechanical stress simulation of vertical silicon fins with unequal oxide deposition on their sidewalls (inner vs. outer). LPCVD simulated using Sentaurus Topography 3D; mechanical stress computed by Sentaurus Interconnect: 3D (a) and 2D cut (b) stress distribution.

Electrostatic Field Computation with Sentaurus Device

It is possible to use Sentaurus Topography 3D together with Sentaurus Device to simulate the electrical behavior of devices whose geometry strongly depends on critical topography processes.

Figure 5 shows the electrostatic field distribution computed by Sentaurus Device for a complex 3D stacked NAND-flash structure (BiCS technology), whose profile has been computed using Sentaurus Topography 3D.

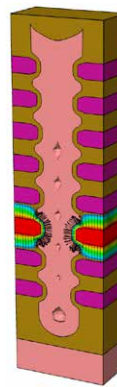


Figure 5: Study of a complex 3D stacked NAND-flash structure (BiCS technology) using Sentaurus Topography 3D. The electrostatic field was simulated using Sentaurus Device.

References

- [1] Sentaurus Topography 3D User Guide, Version H-2013.03, Mountain View, CA: Synopsys, Inc., 2013.
- [2] T. K. Chini et al., "The angular dependence of sputtering yields of Ge and Ag," *Nuclear Instruments and Methods in Physics Research Section B: Beam Interactions with Materials and Atoms*, vol. 72, no. 3–4, pp. 355–358, 1992.
- [3] T. Mizuno et al., "Analytical Model for Oblique Ion Reflection at the Si Surface," *IEEE Transactions on Electron Devices*, vol. 35, no. 12, pp. 2323–2327, 1988.

Sentaurus Device

Mobility Models Updates

ThinLayer Mobility Model Enhancements

The **ThinLayer** mobility model in Sentaurus Device is a physics-based model that explicitly accounts for the dependency on layer thickness. This model can be used for the accurate simulation of advanced transistors such as ultrathin-body SOI MOSFETs, double-gate FETs and FinFETs that have silicon layers whose thickness can be as small as a few nanometers.

The original implementation of the **ThinLayer** mobility model in Sentaurus Device was based on the model described by Reggiani et al. [1] and the Sentaurus Device Lombardi model. The model has the attractive feature that, for small layer thicknesses, it agrees well with the Reggiani model and, for large layer thicknesses, it reduces to the well-calibrated Lombardi model.

The **ThinLayer** model has been reimplemented in Sentaurus Device, so that it can be used in conjunction with the inversion and accumulation layer mobility model (**IALMob**) as an alternative to the Lombardi model. In the **IALMob** case, the model also retains agreement with the Reggiani model for small layer thicknesses and reduces to **IALMob** for large layer thicknesses.

Additional enhancements have been made to the **ThinLayer** model to support the simulation of devices such as FinFETs that can have channel regions with more than one surface orientation. For example, the **ThinLayer** model now supports the auto-orientation framework and the use of named parameter sets. The auto-orientation framework allows Sentaurus Device to automatically switch to different orientation-dependent model parameter sets based on the surface orientation of the nearest interface.

In addition, the **ThinLayer** model has been extended to include an enhanced thickness fluctuation component that provides improved accuracy for large normal electric fields. The **ThinLayer** model, with this extension, has been calibrated against single-gate SOI measurement data for (110) surface orientations (see Figure 1). The calibrated parameters can be found in the **ThinLayerMobility "110"** parameter set in the **Silicon.par** file located in the directory **\$STROOT/tcad/\$TRELEASE/lib/sdevice/MaterialDB**.

Finally, the thickness extraction of the **ThinLayer** mobility model can now account for mirror-image symmetries. This allows the use of the **ThinLayer** mobility model when simulating only half of a symmetric structure. This is especially important for reducing the node count and simulation times for large 3D structures, such as FinFETs.

release allows Sentaurus Device to take the symmetry into account so that it can extract the correct thickness even when only half of the symmetric structure is simulated. Users no longer have to choose between the thin layer mobility model and speed; now they can have both.

Enhancements to the eSubband and hSubband Models

Several improvements were made to the physics-based eSubband and hSubband models which are used for stress-induced, inversion-layer mobility gain. In particular, to improve accuracy for certain orientations, enhancements were made in the carrier scattering model to better account for intra- and inter-valley phonon scattering. Additional calibration and verification was also performed against Kubo-Greenwood calculations, and runtime was reduced for holes by providing an option to save and load pre-computed band data.

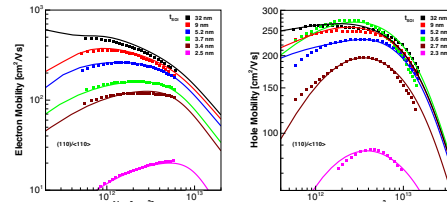


Figure 1: Comparison of experimental data [2], [3] for (110)-oriented single-gate SOI devices (symbols) with Sentaurus Device simulated results using the **ThinLayer mobility model (lines).**

Symmetry Operations in Thin layer Mobility Model

Many devices are symmetric. For example, FinFETs often have a vertical symmetry plane that runs along the channel. As FinFETs usually must be handled as 3D devices, it is attractive to speed up the simulation by using only half of the simulated structure. Previously this was not possible when using the thin layer mobility model: Sentaurus Device did not know about the assumed symmetry and, therefore, could not extract the fin width correctly. The new

Impedance Field Method (IFM)

The capabilities for geometric variations have been significantly extended. In previous releases, only the variations of semiconductor-insulator and insulator-insulator interfaces were supported. In this new release, the position of contacts on insulators and of metal-insulator interfaces can also be handled. This allows the description of variations at metal gates without the need for difficult workarounds. Furthermore, geometric variations can now also be used with the statistical IFM. In addition to Gaussian variations, geometric variations with statistical IFM also support exponential and grain-like correlations. When making a variation to a structure simulated in 2D, you can also perform the variation in 2D. For example, moving a point in 2D corresponds to moving a line. For variation analysis, this is usually not desired. For noise-like IFM, previous versions of Sentaurus Device already made sure that variations are handled as 3D variations, i.e.



the 2D structure is first internally extruded and then the variation is applied 3D. For the statistical IFM, this was only true for doping and trap concentration variation, which do not have spatial correlation. The new release adds a keyword `ExtrudeTo3D`, which will assure that statistical IFM can be used in 2D for correlated variations (geometric and workfunction). `ExtrudeTo3D` performs the randomization of the structure in 3D for an internally extruded device. While this 3D randomization takes longer runtime than the (unphysical) 2D randomization, all other computational steps (in particular, solving the nonlinear systems and computing the Green functions) are as fast as for 2D. For typical cases, this means that `ExtrudeTo3D` achieves 3D accuracy at nearly 2D speed.

Although IFM simulations are performed in the AC analysis framework, only the zero-frequency behavior is of interest. Starting with Sentaurus Device H-2013.03 users can specify zero as the starting and ending frequency for the AC analysis. These settings suppress the computation of the imaginary part of the Green's function (which vanishes for low frequencies). The advantage is a faster computation time and less memory usage for the Green's function computation. At zero frequency, however, the voltage Green's function becomes ill defined for devices with isolated AC nodes, such as the gate of a MOSFET. Because of such devices, by default, the computation of the voltage

Green's functions (and related response quantities) is suppressed when using the zerofrequency mode. However, for devices without isolated AC nodes, the voltage Green's functions are all well defined, and their computation can be switched on using the `VoltageGreenFunctions` keyword.

Within the statistical IFM Sentaurus Device computes the difference in currents δI between the reference device and a device which is randomly perturbed according to the considered variability source. Because δI is computed within linear response some post-processing is needed to accurately construct the IV characteristics of the randomized devices from δI . Also within the statistical IFM we consider a large set of randomizations—typically about 10,000 per variability source. Thus post-processing is also needed for the statistical analysis of this large amount of data.

Sentaurus Visual H-2013.03 includes an IFM Post Processing Support Library to manage and analyze IFM data. In particular, this library supports the construction of the individual I_dV_g characteristics of a randomized MOSFET. Also the construction of the randomized Voltage Transfer Characteristics of an inverter or SRAM cell is supported. This library further allows users to conveniently apply standard statistical analysis methods to the IFM data such as computing and visualizing statistical distributions, computing their moments and comparing them to a

Gaussian distribution. The library allows the analysis of the effect of each variability source separately or as combined effects for several variability sources. This can be done via post-processing the IFM output of single Sentaurus Device simulations.

Figures 2-4 show statistical IFM results for an n-type FinFET obtained by using the aforementioned new IFM features: gate oxide thickness roughness is simulated using

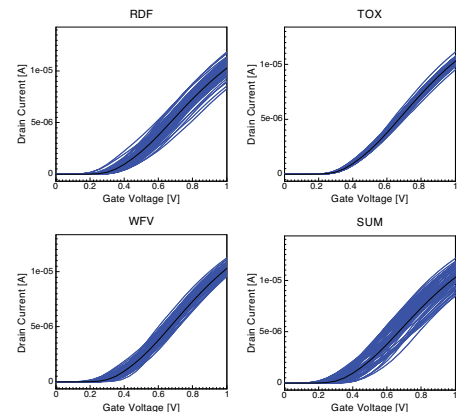


Figure 3: NMOS I_d - V_g curves for first 50 randomizations of the reference MOSFETs for $V_d = 50$ mV for the variability sources random dopant fluctuations (RDF), gate oxide thickness roughness (TOX), workfunction variability (WVF), and the combined effect of all three sources (SUM). Black dashed line is reference device.

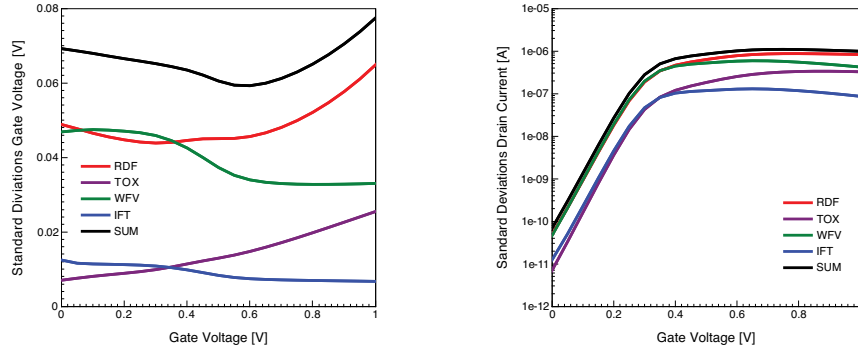


Figure 2: Gate voltage and drain current standard deviations for a n-type FinFET for drain bias of 50 mV as computed from statistical IFM. Results are given for the individual variability sources as well as the combined effect of all three sources. Red: random dopant fluctuations (RDF), purple: gate oxide thickness roughness (TOX), green: workfunction variability (WVF), blue: interface trap concentration variability (IFT), and black: combined effect of all three sources (SUM).

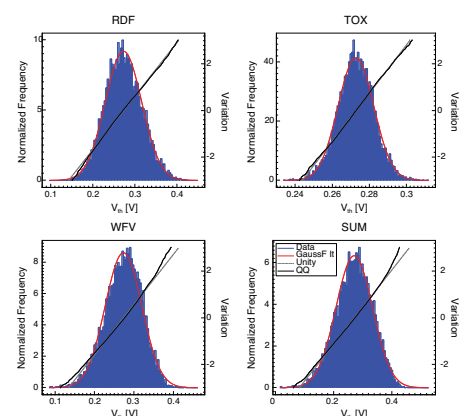


Figure 4: NMOS linear threshold voltage histograms created from threshold voltages extracted from individual I_d - V_g curves shown in Figure 2. The solid black line shows the quantile-quantile plot that compares the histogram to a Gaussian distribution. Any deviation from the gray unity line indicates a derivation from a perfect Gaussian.

the new geometric variations capabilities in statistical IFM. Both, the workfunction variability and the gate oxide thickness roughness are applied to the high-K/gate contact interface. The AC simulations are performed at zero frequency. Also all post-processing is performed by the Sentaurus Visual IFM Post Processing Support Library. Application Notes which showcase the new IFM related features examples are available on SolvNet [4][5].

Dynamic Nonlocal Path Band-to-Band Model

The dynamic nonlocal path band-to-band model is popular for the simulation of tunneling FETs and other devices in which the band-to-band tunneling path changes with bias condition. Depending on the materials, mole fractions, and operating conditions, multiple processes can contribute to the tunneling rate. Previous releases allowed up to three different processes to be handled. To support even more complicated devices, the new release allows an unlimited number of different processes. Furthermore, these processes are distinguished by names chosen by the user, rather than by a number. Therefore, by choosing meaningful names, users can keep the parametrization more manageable.

Nonlocal PMI

The physical model interface (PMI) in Sentaurus Device provides direct access to various models in the semiconductor transport equations. The user implements new C++ functions that evaluate these models and Sentaurus Device loads these functions at run-time using the dynamic loader.

Most of the existing PMIs, such as avalanche generation or mobility, are vertex-based. They are invoked for each mesh vertex to evaluate the model values and their derivatives. Sentaurus Device uses these vertex-based models self-consistently during the Newton algorithm.

In contrast to the vertex-based PMIs, a few of the existing PMIs are mesh-based. They are supported by a rich set of functions to access the device mesh:

- ▶ The mesh can be traversed in various ways. It is possible to loop over all vertices, edges, elements, regions, or region interfaces, as necessary.
- ▶ The run-time support functions provide access to the connectivity of the mesh. It is easy to find the edges terminating at a particular vertex, or the elements connected to a particular edge, for example.

A mesh-based PMI computes its values based on data fields defined on the mesh:

- ▶ Constant fields, such as doping concentration or mole fractions, are available.
- ▶ The basic solution variables, such as electrostatic potential or carrier densities, are available.
- ▶ The data from the box method discretion can be accessed, such as vertex measures or edge coefficients.

Examples of mesh-based PMIs include the current plot PMI and the hot-carrier injection PMI. So far, mesh-based PMIs have only been used during post-processing since they did not provide the derivatives required by the Newton algorithm.

With the H-2013.03 release Sentaurus Device offers a nonlocal PMI, which is a new class of mesh-based PMIs that can be used self-consistently during the Newton algorithm. A nonlocal PMI represents a more advanced interface compared to a post-processing PMI. Therefore it requires the implementation of additional user functions:

- ▶ The PMI must provide a list of dependencies. For example, a nonlocal PMI may depend on electron and hole densities, as well as the effective intrinsic density.
- ▶ The dependencies of the model values on the input variables must be declared. For example:

- The model value in vertex 17 depends on
 - Electrostatic potential in vertex 22
 - Electron density in vertex 15
- The model value in vertex 18 depends on
 - Hole density in vertex 25
 - Lattice temperature in vertex 7
- ▶ The model values and their derivatives must be evaluated during the Newton iteration.

In the H-2013.03 release Sentaurus Device introduces a nonlocal generation-recombination PMI as a first example of a nonlocal PMI. This PMI provides access to the recombination rates R_n and R_p in the continuity equations:

$$\nabla \vec{J}_n = qR_n + q \frac{\partial n}{\partial t}$$

$$-\nabla \vec{J}_p = qR_p + q \frac{\partial p}{\partial t}$$

Usually, the electron and hole recombination rates are chosen identical to ensure carrier conservation. In the context of the nonlocal generation-recombination PMI, however, it is possible to compute different rates for electrons and holes in order to model nonlocal transport processes:

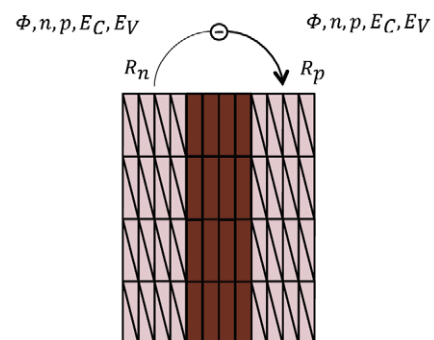


Figure 5: Nonlocal transport

The electron and hole recombination rates R_n and R_p can be computed as functions of the solution variables ϕ , n , and p at the end points of the tunneling path as well as at intermediate points. Similarly, other quantities such as the conduction and valence band energies E_c and E_v can be used in the calculations as well.



The nonlocal PMI also provides an option to recompute the stencil of the Jacobian matrices during the simulations. This may be necessary in the case of tunneling processes, where the tunneling path changes in dependence on the bias conditions of the device.

Arbitrary Doping Species

Starting with the H-2013.03 release Sentaurus Device provides additional flexibility in handling doping species. All dopants are now defined through the file `datexcodes.txt`. Each doping species is identified either as a donor or as an acceptor. It is also possible to restrict doping species to certain substrate materials. For example, in the case of GaN-on-silicon technology, silicon can be declared as a doping species for GaN only. Thus silicon will not be recognized as a dopant within silicon regions.

The file `datexcodes.txt` also establishes the connection between chemical, active, and ionized concentrations. Previously, this information was hardcoded into Sentaurus Device, but now it is accessible in `datexcodes.txt`.

It is now also easier to use group IV elements, such as silicon or germanium, as doping species. Group IV impurities act as amphoteric dopants in III-V compound semiconductors. For example, silicon is an amphoteric dopant in GaAs, because it acts as a donor on a Ga site and as an acceptor on a As site. In order to handle such situations more easily, the file `datexcodes.txt` defines `nSiliconConcentration` as a donor, and `pSiliconConcentration` as an acceptor. The same concept also applies to the remaining group IV dopants, namely, carbon, germanium, and tin.

Box Method Parallelization

Both Sentaurus Process and Sentaurus Device use the box method finite volume approach to discretize their partial differential

equations. As a result the calculation of the box method measures and coefficients can become a computational bottleneck.

In Sentaurus Process the box method must be recomputed whenever the geometry changes. This becomes especially noticeable in the case of 3D oxidation. In Sentaurus Device the box method is usually only computed once at the beginning of a simulation. However, when the self-consistent anisotropic mobility model is enabled together with the `AverageAniso` approximation the box method must be recomputed for each Newton step.

In the H-2013.03 release the box method algorithm has been parallelized in order to improve this situation. On 8 cores, speedup factors larger than three have been observed for sufficiently large problems.

Sentaurus Device Monte Carlo Enhancements

Single-Particle Monte Carlo

The focus for the single-particle Monte Carlo approach in release H-2013.03 has been to increase the usability, to simplify default models for better comparability with the literature (compare e.g. [6]), and to make future extension to new channel materials easier to implement.

Previously, in the presence of stress, Monte Carlo device simulation required the strain tensor in the crystallographic coordinate system as input. Now, as an alternative, the stress tensor in the device coordinate system can also be used where exactly the same syntax as in drift-diffusion simulation is employed for the specification.

Furthermore, acoustic intravalley scattering now relies on the elastic equipartition approximation and ionized impurity scattering is by default based on the Brooks-Herring model calibrated to the Masetti instead of the Caughey-Thomas formula, to improve accuracy at high doping levels.

Sentaurus Band Structure Enhancements

Subband and Inversion-Layer Mobility Calculator

Several new features have been added to Sentaurus Band Structure to enhance the calculation of inversion-layer mobility and to improve the empirical pseudopotential method (EPM) calculation of III-V bulk band structures.

Coulomb scattering has been added to the list of scattering mechanisms that can be used when calculating inversion-layer mobility. Local Coulomb scattering due to bulk impurities as well as remote Coulomb scattering (RCS) due to interface charge can be considered. Remote Coulomb scattering due to interface charge has been identified as one of the major mechanisms responsible for mobility degradation in high-K/metal-gate stacks as well as an important mechanism in some alternative channel materials. At high inversion charge, the screening of Coulomb scattering can be modeled using the original scalar Lindhard dielectric function or using a new tensor-based model that is more suitable for double-gate structures. The Coulomb scattering model essentially has no adjustable parameters since it automatically detects all specified bulk and interface charge in the structure.

Due to improved transport properties relative to silicon, silicon germanium (SiGe) is now being considered as an alternative channel material for advanced CMOS technology. To enable electron mobility calculations for SiGe nMOS, several improvements have been made to the inversion-layer mobility calculation feature in Sentaurus Band Structure. In particular, based on empirical pseudopotential calculations, a mole fraction dependent framework for the band parameters of the Δ , Γ , and L valleys has been created. For mobility calculations, a similar framework has been created for the phonon, surface roughness, alloy, and Coulomb scattering models. With new scattering parameters calibrated to select



literature data, this framework enables the calculation of nMOS SiGe mobility for arbitrary mole fraction, stress, and orientation. For example, Fig. 6 demonstrates good agreement between calculated results and experimental data for a relaxed Ge (001)/<110> nMOS structure.

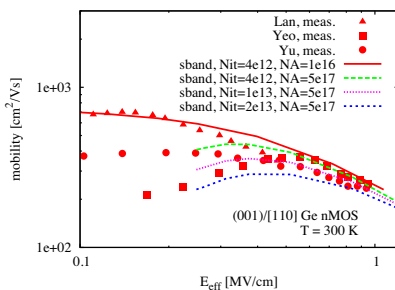


Figure 6: Comparison of Ge electron mobility calculations in Sentaurus Band Structure to experimental data [7,8,9] for a relaxed Ge (001)/<110> nMOS structure.

The EPM for computing bulk band structure has been extended and calibrated to enable the calculation of band structure for select III-V materials. In particular, the mole fraction dependence of the local pseudopotential and spin-orbit models has been generalized to enable measured data for key band parameters such as valley splitting and effective mass to be accurately reproduced. Calibrated parameters are now provided for InGaAs and InGaSb enabling the calculation of bulk band structure for these materials for arbitrary mole fraction and strain.

Enhancements for Optoelectronic Applications

Several new optical features have been introduced in Sentaurus Device to enhance the simulation capabilities for CMOS image sensors and solar cells. Under the unified optical generation interface, imported optical generation profiles in TDR format can be truncated, shifted and automatically interpolated to allow for more flexible integration between optical and electrical solutions. In the `ComputeFromSpectrum` feature, simple TCL expressions can be used to control and select the range

of wavelengths for ramping and other constraints. A periodicity can also be defined for a transient optical light pulse so that the pulse can be repeated in a regular cycle. Finally, the online tutorial has been extended by a section about the unified optical interface, providing users with an efficient introduction.

Several improvements have been implemented for the raytracer. In the user input rays feature, one can now specify the polarization vector selectively or choose a randomized polarization. Periodic boundary conditions have been introduced to enable simulation of periodicity in the parallel x, y and/or z directions. An improved weighted interpolation scheme can also be used to distribute the optical absorption from rays to vertices, resulting in a more accurate representation of the optical absorption profile. The diffuse boundary condition has an added capability of reading and utilizing a wavelength dependent table of reflectivity and transmittivity values.

Important models have been introduced in Sentaurus Device EMW. Figure 7 shows the excitation of diverging Gaussian beams without the requirements that the waist of the beam be centered at the excitation plane.

Modified Lorentz and modified Drude-Lorentz dispersive models have been added to enable better fitting of the wavelength dependent complex refractive indices over a wider range in dispersive simulations. These are advanced topics and users are advised to contact TCAD Support before using the dispersive features.

References

- [1] S. Reggiani, E. Gnani, A. Gnudi, M. Rudan, and G. Baccaran, "Low-Field Electron Mobility Model for Ultrathin-Body SOI and Double-Gate MOSFETs With Extremely Small Silicon Thicknesses," *IEEE Trans. Electron Devices*, vol. 54, no. 9, pp. 2204-2212, Sep. 2007.
- [2] G. Tsutsui and T. Hiramoto, "Mobility and Threshold-Voltage Comparison Between (110)- and (100)-Oriented Ultrathin-Body Silicon MOSFETs," *IEEE Trans. Electron Devices*, vol. 54, no. 10, pp. 2582-2588, Oct. 2006.
- [3] G. Tsutsui, M. Saitoh, and T. Hiramoto, "Experimental Study on Superior Mobility in (110)-Oriented UTB SOI pMOSFETs," *IEEE Electron Device Lett.*, vol. 26, no. 11, pp. 836-838, Nov. 2005.
- [4] *Modeling Random Variability Effects with the Statistical Impedance Field Method*, TCAD Sentaurus Application Note, available from SolvNet at <https://solvenet.synopsys.com/retrieve/039155.html>, March 2013.
- [5] *Modeling Statistical Variability of Static Noise Margins of SRAM Cells Using the Statistical Impedance Field Method*, TCAD Sentaurus Application Note, available from SolvNet at <https://solvenet.synopsys.com/retrieve/039390.html>, May 2013."
- [6] M.-J. Chen et al., "Effect of Strained k.p Deformation Potentials on Hole Inversion-Layer Mobility," *IEEE Trans. Electron Devices*, vol. 60, no. 4, pp. 1365-1371, 2013.
- [7] H. -S. Lan et al., "Electron scattering in Ge metal-oxide-semiconductor field-effect transistors," *Appl. Phys. Lett.* 99, 112109 (2011).
- [8] C. C. Yeo et al., "Electron Mobility Enhancement Using Ultrathin Pure Ge on Si Substrate," *Electron Device Lett.*, vol. 26, no. 10, 2005.
- [9] D. S. Yu et al., "Fully Silicided NiSi:Hf-LaAlO₃/SG-GOI n-MOSFETs With High Electron Mobility," *Electron Device Lett.*, vol. 25, no. 8, 2004.

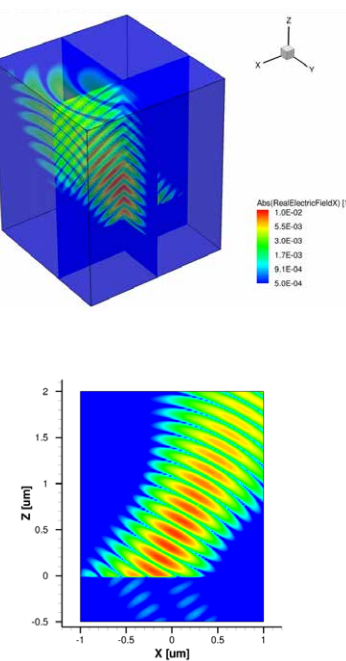


Figure 7: Electric field distribution for an oblique Gaussian beam.



Sentaurus Interconnect

Fracture Mechanics Enhancements

Additions have been made to extend J integral calculations for plastic materials and to improve performance of cohesive zone material model.

J Integral for Plastic Materials

Cracks in ductile materials like metals or alloys deform plastically under high stresses around the crack tip. The `j_integral` command can now be used to compute J integral values for such cracks. Prior to computing the J integral, a stress analysis with monotonic loading should be performed using the deformation plasticity model for the material with crack.

As an example, J integral calculations are performed for a rectangular metal plate ($H = 10 \mu\text{m}$, $W = 5 \mu\text{m}$, $B = 2.5 \mu\text{m}$) with an edge crack ($a = 2.5 \mu\text{m}$) subject to thermal gradient (136K to 464K) along the width [1]. A fine mesh ($0.125 \mu\text{m}$) is used for better resolution of stresses around crack tip.

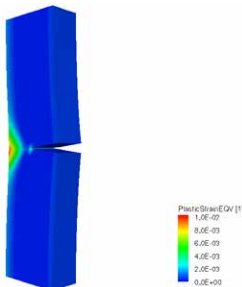


Figure 1: Equivalent plastic strains for rectangular plate with edge crack

Figure 1 shows equivalent plastic strain contours on deformed a plate. Contours show higher strains around the crack tip and near the middle of the opposite edge. J integral calculations are performed over multiple domains around the crack tip but away from the opposite edge.

Table 1 shows the values over all domains and at different points along the thickness. Results from a two dimensional plane strain model are used as a reference.

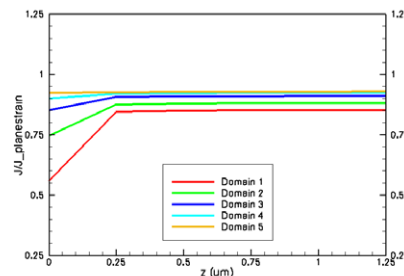


Figure 2: Plot of $J/J_{\text{planestrain}}$ at different points along thickness for different domains.

A plot of the values over the full thickness is shown in Figure 2. The variation in values near the surfaces is attributed to boundary effects.

Cohesive Zone Material

The cohesive zone material (CZM) model is used for simulating crack propagation along a predefined path. A predefined crack is assumed to be initially closed with the opposing surfaces held together by cohesive forces. Separation of crack surfaces under external loads or boundary

conditions is governed by the cohesive zone material law that defines the relationship between cohesive traction and separation. The nonlinear solution for crack surface separation is obtained by using Newton iterations with automatic time stepping and convergence checks.

To demonstrate the improvements to CZM model, delamination in a double cantilever beam specimen is simulated using the Exponential Law with two-dimensional and three-dimensional models and results for traction and separation are compared to experimental data [2].

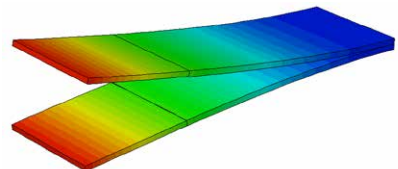


Figure 3: 3D model of a double cantilever beam specimen—deformed shape.

The double cantilever beam (DCB) specimen, as shown in Figure 3, consists of two rectangular strips of composite material bonded together. The specimen is held fixed on the right end and equal but opposite displacements are applied on top and bottom faces at the left end.

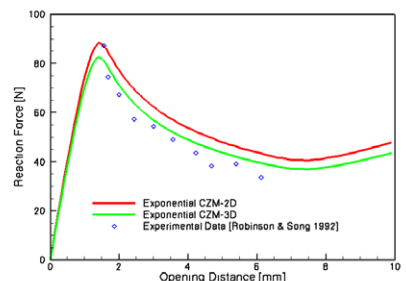


Figure 4: Reaction force vs. opening distance for double cantilever beam specimen.

Domain	$z=0.0$	$z=B/10$	$z=B/5$	$z=3B/10$	$z=2B/5$	$z=B/2$
1	0.5599	0.8451	0.8496	0.8507	0.8512	0.8516
2	0.7453	0.8750	0.8792	0.8801	0.8805	0.8808
3	0.8515	0.9050	0.9082	0.9090	0.9094	0.9097
4	0.8992	0.9187	0.9216	0.9223	0.9227	0.9230
5	0.9233	0.9240	0.9267	0.9274	0.9278	0.9281

Table 1: $J/J_{\text{planestrain}}$ for rectangular plate



The reaction force at the point of application of displacement boundary is plotted against the displacement as shown in Figure 4. The results show good agreement with data from experiment. Small differences can be attributed to differences in boundary conditions and mesh used for simulation.

New Material Models

Sentaurus Interconnect H-2013.03 implements three new material models have been added to extend the mechanics capabilities.

Deformation Plasticity

Deformation plasticity can be used to model plastic behavior in materials that do not have well defined yield stress. This model can only be used with monotonic loading. It is commonly used to model plastic deformation around crack tips for J integral calculation.

Swelling

This material model is provided to simulate temperature dependent volumetric expansion of material. The material behavior is defined by linearly interpolating tabular data of strain rates at different temperatures. It can be used for various applications that include nonlinear thermal expansion or where volumetric expansion is an indirect function of temperature, e.g., swelling of polymer materials with temperature due to diffused moisture.

Power Law Creep

Power law creep is a commonly used material model suitable for simulating steady state creep in alloys like solder. When used by itself, it models viscous behavior in the material. It can also be used in combination with incremental plasticity to model viscoplastic behavior.

An example problem with a single solder ball is used to demonstrate creep and swelling material models. Figure 5 shows the geometry of the structure with symmetry boundaries on all surfaces except top. A cyclic temperature loading (as shown in Figure 6) is applied to simulate service conditions.

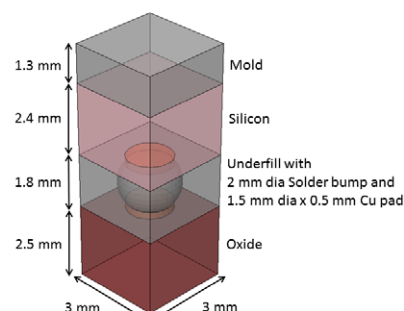


Figure 5: 3D model of a solder ball in a flip chip.

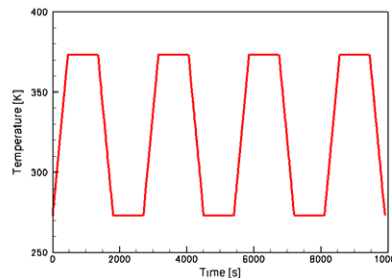


Figure 6: Time varying temperature loading.

Solder material is modeled using creep with plasticity. Copper pads are modeled using the plastic material model. All the other materials are modeled as linear elastic with non-zero thermal expansion. Additionally, the swelling model is used for Mold material to simulate nonlinear volumetric expansion with temperature. Figure 7 shows the swelling strain rate data—separate curves specified for loading and unloading.

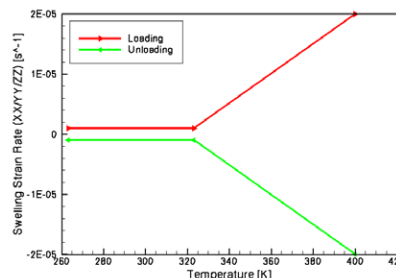


Figure 7: Swelling strain rate vs. temperature data.

Variation of Mises stress in Solder with time is shown in figure 8. Comparison of stress variation in Figure 4 with temperature variation in Figure 6 shows stress relaxation during constant temperature intervals and jump in stress values during cooling and heating intervals.

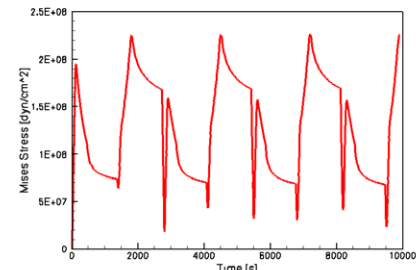


Figure 8: Mises stress variation with time.

Figure 9 shows accumulation of equivalent creep and plastic strains in Solder with time. Equivalent creep strain increases whenever there is a change in temperature and remains constant otherwise. Equivalent plastic strain increases when Mises stress exceeds yield value.

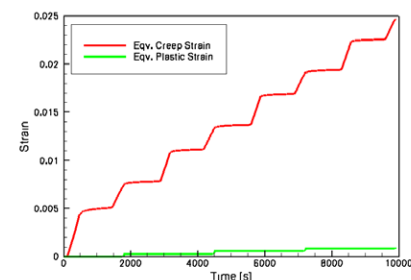


Figure 9: Variation of equivalent creep and plastic strains with time.

Figure 10 shows the cyclic variation of swelling strain (XX component) with time. Due to the nonlinear variation of prescribed swelling strain rates with temperature (as shown in Figure 7) swelling strain varies in a nonlinear manner in each temperature cycle. A drift in values between cycles is attributed to non-uniform time stepping that introduces non-symmetry between the loading and unloading branches of each temperature cycle.

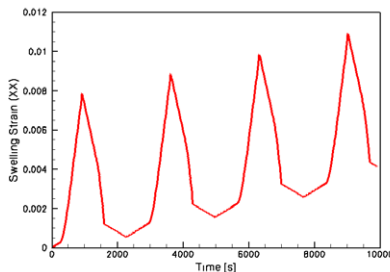


Figure 10: Variation of swelling strain (XX) with time in Mold material.

The results presented above for a simple geometry demonstrate how complex material interactions can be simulated using appropriate material models. Default material parameters are provided for creep for Solder material (96.5Sn3.5Ag) as reported in [3]. Swelling material model interface is designed for empirical data so no parameters are provided.

Second Order Finite Elements

Sentaurus Interconnect H-2013.03 release provides the capability to use second order finite elements for mechanics simulations. In previous releases, linear finite elements have been used for material models. A linear displacement solution over an element in 2D is shown below.

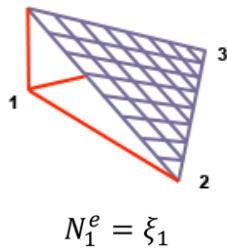


Figure 11: Linear element shape function

The use of second order finite elements provides a quadratic displacement solution over any given element.

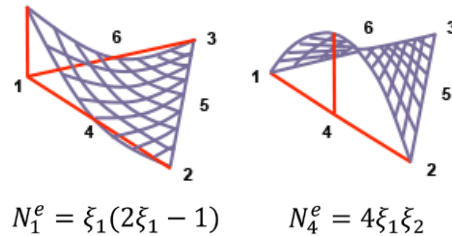


Figure 12: Second order element shape functions.

The second order finite elements provide higher solution accuracy and better stability for certain classes of problems. For example, when considering bending problems, linear elements may lack stability due to element locking. To prevent element locking linearly varying strains are required within the element, which in turn require a quadratic displacement solution. Hence, second order elements are very useful to obtain stable solutions especially when dealing with wafer bending or fin bending problems. The following figure shows the displacement obtained using linear and second order elements for warpage of a plate. It can be seen that the second order solution provides better accuracy and better symmetry of solution.

Second order elements also provide a higher resolution of stress and strain owing to the quadratic displacement solution. The following figure shows the stress distribution over a beam using linear elements as compared to using quadratic elements. The stress for a linear element is constant over an element providing a less accurate picture. However the linear distribution of stress over a quadratic element provides a much better solution.

Support for second order elements has been added to triangular elements in 2D and tetrahedral elements in 3D. The material models supported in this release are elasticity, visco-elasticity and plasticity. Visco-plastic, Creep, Swelling, Crack and Anisotropic material models are currently not supported and under consideration for implementation in future releases.

Although, second order elements provide higher accuracy and stability, it comes at the cost of higher memory requirement and runtime. For the same mesh as used for a linear element the memory requirement for a second order simulation maybe of the order of 4x (in 2D) and 8x (in 3D). The larger numbers of degrees of freedom also lead to increase in runtime of the matrix solver. The solver time for a 3D run may be of the order of about 15x-20x that of a linear element.

Since second order elements provide higher accuracy the simulations are carried out with a relatively coarser mesh (compared to linear element simulation).

Second order elements are also available for sub-modeling. The global and/or local model can be solved with these higher order elements for better accuracy/stability.

Advanced Dirichlet Boundary Conditions

In this release of Sentaurus Interconnect, the previously available Dirichlet boundary conditions have been extended to provide more advanced capabilities, including rotation, along with translation. Now it is possible to apply a rotation, to a side boundary or a contact, about a given point, producing a net displacement as shown in figure below,



Figure 13: Combined translation and rotation applied via advanced Dirichlet boundary conditions.

The displacement applied to a boundary or a contact is calculated as a total displacement at any given point given by,

$$\begin{Bmatrix} v_x \\ v_y \\ v_z \end{Bmatrix} = \begin{Bmatrix} dx \\ dy \\ dz \end{Bmatrix} + \begin{bmatrix} 0 & -rz & ry \\ rz & 0 & -rx \\ -ry & rx & 0 \end{bmatrix} \begin{Bmatrix} x - x_n \\ y - y_n \\ z - z_n \end{Bmatrix}$$

where, x_n , y_n , and z_n are the coordinates of the point around which rotation occurs, dx , dy , dz are the specified translation velocities and r_x , r_y , r_z the rotational velocities.



The figure below shows the result where the right side boundary is simultaneously pulled and rotated about a point located along the center of the right face plane.

Automatic Time Stepping and Convergence Checks

For nonlinear material models like plasticity, viscoplasticity, or cohesive zone material, finite element equations for mechanics need to be solved using Newton iterations for a converged solution. New criteria have been added that check convergence of force, energy and displacement by comparing normed values against reference values. Additional criteria for checking errors in strains are also provided for viscoplastic

material models. All the necessary convergence checks are performed automatically using default reference values and tolerances.

Material nonlinearity also requires the stress analysis to be carried out over several time steps. The initial value and the maximum value of the time step are specified on `solve` command. For optimal performance, a time stepping scheme has been added to automatically adjust the size of the time step based on convergence history and other error checking criteria. In case of a convergence failure, the time step is cut back and repeated.

Use of automatic time stepping and convergence checks improves performance and solution accuracy of nonlinear problems.

References

- [1] C. F. Shih, B. Moran, and T. Nakamura, "Energy release rate along a three-dimensional crack front in a thermally stressed body," *International Journal of Fracture*, vol. 30, no. 2, pp. 79–102, 1986.
- [2] G. Alfano, M. A. Crisfield, "Finite element interface models for the delamination analysis of laminated composites: mechanical and computational issues," *International Journal for Numerical Methods in Engineering*, vol. 50, pp. 1701-1736, 2001.
- [3] S. Wiese, F. Feustel, E. Meusel, "Characterisation of constitutive behaviour of SnAg, SnAgCu and SnPb solder in flip chip joints," *Sensors and Actuators*, A99, pp. 188-193, 2002.

Sentaurus Mesh

Conservative Interpolation

A new conservative interpolation option is added within the `interpolateMesh` utility in the tools module. The conservation is achieved with the intersection of the destination mesh element with source mesh elements, using quadrature formula. This method is computationally intensive as compared to simple linear interpolation as it involves element intersections. By default the simple linear interpolation is used. The conservative interpolation can be activated by specifying the "conservative" flag within the `interpolateMesh` utility section of the command file.

Figure 1 shows three meshes with arsenic concentration. The left mesh is a source mesh. The mesh shown in the middle figure is a coarse mesh with field interpolated from the left source mesh using simple linear interpolation. The mesh in the right figure is the same coarse mesh as shown in the

middle but field interpolated from a source mesh using conservative interpolation. The arsenic concentration integration in the middle mesh obtained using simple linear interpolation deviates by 14% when compared to same field in the source mesh. The same arsenic concentration integration in the right mesh obtained using conservative interpolation deviates by less than 0.5%.

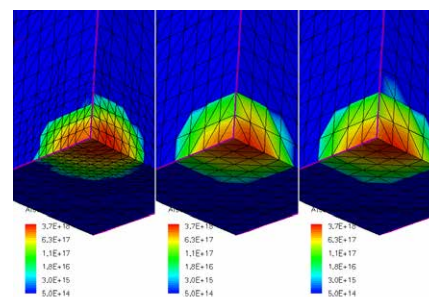


Figure 1: Source mesh (left), mesh with linear interpolation (center), and mesh with conservative interpolation (right).

Screening Scaling Factor in Sano Method

A scaling factor is implemented to the screening factor in the Sano method. This gives users control over the degree of the smoothness of the profile. This scaling factor can be used in the particle definition section and in the doping randomization utility in the tool module. This scaling factor is applied only when `autoScreening` factor is specified. Figure 2 shows three mesh profiles generated with different screening factor k . As the screening scaling factor increases, the smoothness decreases.

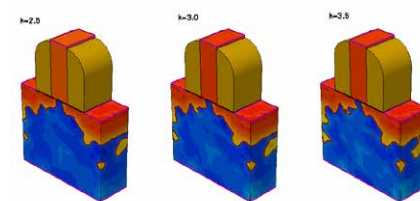


Figure 2: Mesh profiles generated with three different screening factors.



Sentaurus Visual

Sentaurus Visual is a TCAD visualization software. It allows the user interactively analyze and explore data obtained from TCAD simulations. In the new version of Sentaurus Visual, new features have been developed and implemented in order to improve the functionality of the software.

Value Blanking

Value Blanking is a feature that allows visualization only in the areas that are required. It is based on a number of constrains that blank out the fields that meet the target criteria.

A new blanking option called “interpolate vertices” was added in the new version. This option changes the way that the blanking is done resulting in a smoother surface for the data that are displayed. The “interpolate vertices” option takes the vertices of the cells that are between the visualized area and the blanked area and interpolate them, creating new cells that are more accurate in relation with the actual constrains.

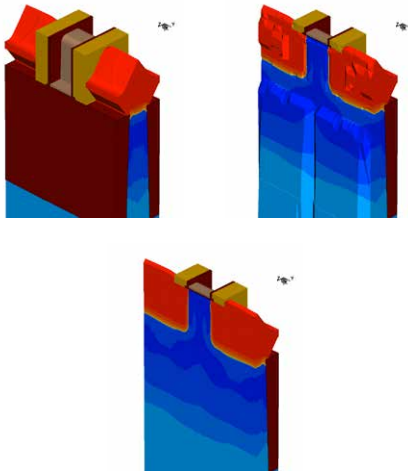


Figure 1: Value blanking used on a FinFET Transistor. Top left: Full structure. Top right: Value blanking with a constrain long the z-axis using the “all vertices” option. Bottom: Smooth surfaces obtained with the “interpolate vertices” option.

The objective of this new option is to obtain flatter surfaces in the areas that limit the blanked area.

Publication Quality 1D Plots

The editing capabilities of text areas and legends in 1D plots have been upgraded to meet the standards of publication quality plots. Mathematical symbols, the Greek alphabet and the definition of subscript and superscripts are now supported. These special symbols can be inserted on any kind of text in 1D plots, such as plot title, axis title, curve labels or axis-tick labels and are written in the form of XML tags that are parsed and converted into the desired symbol.

Also to improve the quality of 1D plots a new option was added for the number format in plot axes. This new option allows displaying numbers in scientific notation.

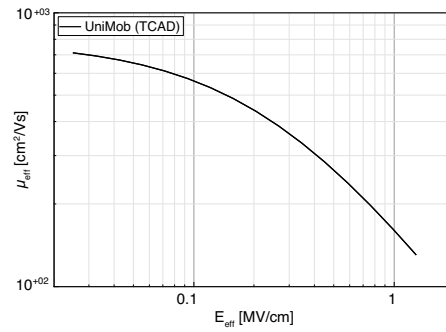


Figure 2: Symbols in axis labels on a 1D plot.

Higher-order Elements

Sentaurus Visual H-2013.03 provides de capability to visualize higher order finite elements in contrast to previous releases that only displayed linear finite elements. New elements available are Serendipity and Gauss elements. Serendipity or second

order elements are cells that have an additional field in the middle of the edges and a quadratic distribution is applied in the element. This provides better resolution for some applications like bending problems.

Gauss elements have multiple field values inside the cell and a linear distribution is used in the element. Second order elements also provide a higher resolution of stress and strain. The stress in the linear elements is constant, resulting in a less accurate solution than the second order elements representation (see also the related Sentaurus Interconnect article in this newsletter). Although higher order elements provide better accuracy and stability, they also consume more memory than linear finite elements when they are applied to the same mesh.

Surface Datasets

Sentaurus Visual now supports the use of dataset on surface elements. This allows the representation of physics characteristics like surface or normal vectors.

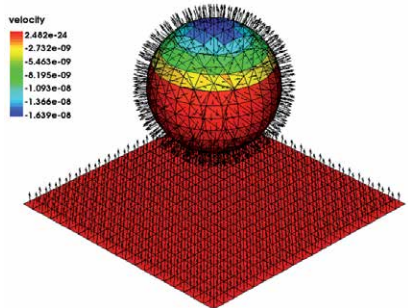


Figure 3: Surface datasets representing normal vectors.

Sentaurus Workbench

Timetable for Run Limits Settings

Sentaurus Workbench manages the utilization of available TCAD Sentaurus licenses and corporate computational resources for a group of users sharing the same installation of TCAD Sentaurus. This goal is achieved by controlling the maximum number of simultaneously running simulations of a certain tool, the so-called run limits.

Previous versions of Sentaurus Workbench allowed the definition of constant run limits for certain tools. Sentaurus Workbench Version H-2013.03 offers much more flexible definition of run limits. Users can define a run limits timetable where run limits depend on the day of the week, the time of the day, holidays, and so on. With the timetable approach, TCAD users can establish a flexible and dynamic run limits schedule taking into account resource availability. Depending on the corporate resource sharing strategy, resource administrators can define run limits on a centralized level (global, site) or allow users to apply their own user-imposed run limits on the user level.

A TCAD installation administrator has full control over run limits settings. When needed, they can forbid the redefinition of global run limits on a user level and they can modify run limits at any time without affecting already running projects. Run limits restrictions that are agreed upon and applied inside a group provide a fair distribution of available licenses between users, as well as the possibility of the temporary concentration of available resources for an urgent job.

Previous versions of Sentaurus Workbench

expected run limits settings to be defined in the tool database. Sentaurus Workbench Version H-2013.03 moves run limits settings from the tool database to a separate XML-compatible file.

Now, run limits settings can be changed during project execution without the risk that some of the running jobs will fail due to checks for consistent file time stamps. Run limits settings can be defined on the global, site, and user levels.

To maintain backward compatibility, Sentaurus Workbench Version H-2013.03 supports old run limits settings specified in the tool database, provided the XML run limits files do not exist yet. However, it is highly recommended to migrate to the new flexible format of run limits settings.

- A project directory contains the file project; it is a Sentaurus Workbench project.
- A project directory is writable; users can create and delete files in the directory.
- Files in the project directory are writable. Sentaurus Workbench checks user permissions for several key project files.

Sentaurus Workbench no longer requires writable projects to be placed under the STDB file hierarchy. Attached roots can contain writable projects. Only user/group permissions and project configurations define whether a project can be made writable.

New Requirements for Writable Projects

Previous versions of Sentaurus Workbench required a writable or executable project to be stored under the STDB hierarchy. Otherwise, Sentaurus Workbench would handle a project as read-only and display the message "out of STDB", despite the project being writable in terms of user permissions. Sentaurus Workbench Version H-2013.03 removes this restriction and changes the requirements for writable projects. Sentaurus Workbench projects must be placed in a disk-writable area to edit, preprocess, and execute those projects.

Sentaurus Workbench recognizes a disk-writable area by analyzing user permissions of a project directory and project files. A writable Sentaurus Workbench project must meet the following criteria: